Investigation of Stress Field and Fracture Development During Shale Maturation Using Analog Rock Systems

B. Vega[1] · J. Yang[1] · H. Tchelepi[1] · A. R. Kovscek[1]

Abstract

The emergence of hydrocarbons within shale as a major recoverable resource has sparked interest in fluid transport through these tight mudstones. Recent studies suggest the importance to recovery of microfracture networks that connect localized zones with large organic content to the inorganic matrix. This paper presents a joint modeling and experimental study to examine the onset, formation, and evolution of microfracture networks as shale matures. Both the stress field and fractures are simulated and imaged. A novel laboratory-scale, phase-field fracture propagation model was developed to characterize the material failure mechanisms that play a significant role during the shale maturation process. The numerical model developed consists of coupled solid deformation, pore pressure, and fracture propagation mechanisms. Benchmark tests were conducted to validate model accuracy. Laboratory-grade gelatins with varying Young's modulus were used as scaled-rock analogs in a two-dimensional Hele-Shaw cell apparatus. Yeast within the gelatin generates gas in a fashion analogous to hydrocarbon formation as shale matures. These setups allow study and visualization of host rock elastic-brittle fracture and fracture network propagation mechanisms. The experimental setup was fitted to utilize photoelasticity principles coupled with birefringence properties of gelatin to explore visually the stress field of the gelatin as the fracture network developed. Stress optics image analysis and linear elastic fracture mechanics (LEFM) principles for crack propagation were used to monitor fracture growth for each gelatin type. Observed and simulated responses suggest gas diffusion within and deformation of the gelatin matrix as predominant mechanisms for energy dissipation depending on gelatin strength. LEFM, an experimental estimation of principal stress development with fracture growth, at different stages was determined for each gelatin rheology. The interplay of gas diffusion and material deformation determines the resulting frequency and pattern of fractures. Results correlate with Young's modulus. Experimental and computed stress fields reveal that fractures resulting from internal gas generation are similar to, but not identical to, type 1 opening mode.

Keywords Shale rock maturation · Analog rock systems · Phase-field fracture propagation model · Stress field · Gelatin

---

B. Vega and J. Yang have contributed equally to this work.

✉ B. Vega
  bolivia@stanford.edu

Extended author information available on the last page of the article

List of Symbols

A	Cross-sectional area (m^2)
b	Biot coefficient (1)
D	Diffusion coefficient (m^2/s)
E	Francfort–Marigo energy functional (J)
E_m	Young's modulus (Pa)
e	Infinitesimal strain tensor
f_σ	Stress-fringe factor (N/mm/fringe)
G_c	Critical energy release rate (J/m^2)
k	Permeability tensor (m^2)
K	Bulk modulus (Pa)
K_{dry}	Drained bulk modulus
K_c	Fracture toughness (Pa$\sqrt{m}$)
K_d	Darcy permeability (nD)
K_I	Stress-intensity factor (Pa$\sqrt{m}$)
h	Sample thickness (m)
H_c	Length of host matrix (m)
H_i	Length of fracture i (m)
l	Fracture length (m)
L	Length of sample (m)
M	Biot modulus (Pa)
N	Fringe order
OL	Ordinary light
P_e	Elastic pressure (Pa)
P_p	Propagation pressure (Pa)
PL	Polarized Light
q	Fluid source term (kg/s)
r	Radius from crack tip to stress element (m)
Re	Reynold's number
S_{av}	Average fracture spacing (m)
W_c	Width of host matrix (m)
u	Displacement field (m)
u_f	Fracture velocity (m/s)
V_i	Dead volume (m^3)
w	Fracture opening (m)
w_f	Fracture thickness (m)
y	Fracture width (m)
α_d	Pulse decay semilog slope (s^{-1})
β	Gas compressibility (Pa^{-1})
ϵ	Length-scale parameter (m)
φ	Phase-field variable (1)
Φ	Strain energy density (J)
γ_s	Surface energy (J s^{-1})
Γ	Crack surface area (m^2)
ρ	Density (kg/m^3)
η	Viscosity (Pa s)
σ	Biot effective stress (Pa)
σ_i	Principal stress in i direction (Pa)
σ_{total}	Total stress (Pa)

ϑ Angle of stress element (°)
ϑ_{ss} Steady-state time (s)
ν Poisson ratio

1 Introduction

The term 'shale' is broadly used to describe a fine-grained sedimentary rock with large amounts of organic material, or kerogen, that is capable of generating petroleum under appropriate conditions of heat and pressure (McCarthy et al. 2011). Source rock thermal maturity is one of the key properties of the formation. It is tied to hydrocarbon generation capacity and yield. Thermal maturation of source rock spans a complex sequence of thermodynamic processes that result in decomposition of the organic matter into light and heavy hydrocarbon fractions and into gas and liquid phases. Maturation is determined by the geological burial conditions of the formation, temperature, pressure, and time, where time is on the order of a few tens or hundreds of million years (Allix et al. 2011). A number of kinetic models that describe source rock maturation in terms of the transformation of kerogen into oil and gas have been proposed by Burnham and Singleton (1983), Bostrom et al. (2009), Burnham (2010), and Le-Doan et al. (2013), among others. Thermal maturation can also be artificially induced through industrial processes such as retorting (American Association of Petroleum Geologists 2016).

The incremental production of liquid and gaseous phases due to source rock maturation involves a cumulative increase in pore pressure that eventually prompts changes in the modulus and distribution of the strain energy of the rock. Fracturing deformation is one of the energy dissipation processes potentially triggered by organic matter and kerogen heat-induced outgassing. A number of studies found that fracture formation constitutes a significant mechanism that increases permeability and provides secondary migration pathways for the maturation-generated hydrocarbons. Capuano (1993) studied the shales in the Oligocene Frio Formation in Texas and determined microfractures were most likely the main supporters of flow. Authors du Rouchet (1981), Talukdar et al. (1988), Özkaya (1988), and Márquez and Mountjoy (1996) proposed microfractures as a by-product of catagenesis. Berg and Gangi (1999) proposed equations for pressure change within source rocks, citing fracturing by gas or oil as a possible mechanism for migration from initially low-permeability source rocks. Lash and Engelder (2005) tied microcrack propagation to the pressure buildup consequence of kerogen maturation.

A numerical modeling approach to the fracture propagation problem posed by shale maturation fracture network development becomes fundamental in order to characterize predictably the material failure mechanisms that play a significant role. The foundation of theoretical linear fracture mechanics is inspired by the pioneering work of Griffith (1921) who showed that a simple stress criterion is *not* sufficient for prediction of fracture propagation. He argued that the so-called critical energy release rate controls whether a fracture is able to propagate along a pre-defined path. The model shows exceptional agreement with laboratory results of brittle materials, such as glass. In the later work of Irwin, plastic dissipation is also included to provide a more realistic description of ductile materials. He also showed that the energy release rate is related to the stress intensity factor (Irwin 1948). There are various models to predict the fracture propagation path by linking it to different stress components in different crack opening modes (Erdogan and Sih 1963). These correlations, however, do not universally apply to all problems.

There are some limitations, however, to Griffith's original energy criterion (Griffith 1921): It cannot handle the initiation of cracks; it requires a pre-defined crack—the propagation direction and crack trajectory are not addressed; crack jumps and branching cannot be modeled, although later there are ad-hoc treatments of branching for some limiting cases. These issues are tackled in more recent work (Francfort and Marigo 1998). They propose a variational approach to fracturing that does not require a preexisting fracture tip or pre-defined path. The crack initiation and path are quantified by minimizing an energy functional. Additionally, this variational fracture criterion was regularized by Bourdin et al. (2000, 2008) where a crack is approximated by a functional originally formulated by Ambrosio and Tortorelli (1990). Later on, a similar model was constructed with a different approach and coined a 'phase-field' model (Miehe et al. 2010a).

Classical computational fracture mechanics models often assume a strong discontinuity to represent a discrete crack. Such models [for example, cohesive zone models, eXtended finite element (XFEM), embedded finite element (EFEM), and discrete fracture (Matrix DFM)] are well adapted to model single fracture propagation in this scenario (Chen et al. 2009; Mohammadnejad and Andrade 2016; Jiang and Yang 2018). The phase-field method of modeling fracture propagation has the advantage of being capable of modeling multiple fractures under branching and merging conditions. Especially in a geological context, a propagating fracture has the potential to merge with preexisting fractures. Importantly, phase field modeling has been applied to hydraulic fracturing (Bourdin et al. 2012; Chukwudozie et al. 2019) and extended to modeling two-phase flow in fractured and poroelastic media (Lee et al. 2018).

The fracture network topology generated from numerical simulation and experiments allows us to investigate further the evolution of effective permeability during the fracture propagation process. For example, Wu et al. (2010) demonstrated the significant impact of rapid fluid flow in fractures on a fractured porous medium using boundary-layer theory. With the aid of statistical descriptions such as fracture aperture, fracture density and connectivity, the uncertainty associated with percolation is quantified, as illustrated by Ji et al. (2011) for example.

The study of the onset and growth of a drainage fracture network within the source rock also calls for a battery of experimental data to validate the aforementioned numerical model, quantify contributions of various parameters, create physical understanding, as well as to reveal variable correlations. One of the challenges is to produce a set of results that can be numerically and dynamically described within a controllable and observable length scale and at a timescale that is not geologic.

The use of analog materials for the purpose of experimental modeling of processes is a common practice in several science and engineering disciplines. An analog is a simplified representation of a more complex system that has scalable and comparable properties to those of the modeled material. An ideal scaled experiment must have an analog material that obeys geometric, kinematic, and dynamic similarity with its natural counterpart (Hubbert 1937). Geosciences frequently employ analogs, such as gelatin, to study Earth crust fracture mechanics and crack propagation. Previous studies have pertained to magmatic intrusions (dykes and sills) and volcanic feeder systems (Kavanagh et al. 2006, 2015; Watanabe et al. 2002; Takada 1990) as well as upper crustal deformation (Di Giuseppe et al. 2009).

Gelatin is a polypeptide formed from the hydrolytic degradation of pig-skin collagen (Ross-Murphy 1992). It is a frequently used analog due to its spectrum of viscoelastic properties that are tunable to emulate the Earth's crust brittleness and elasticity. This behavior is frequently described as a function of gelatin concentration and temperature, among other

variables. At cool temperatures, $T \sim 5$–10 °C, it is in the solid 'gel' state, where the elastic behavior dominates and the viscous component is negligible on short-to-moderate timescales (Kavanagh et al. 2013). Gelatin at high concentrations (i.e., > 3 wt%), behaves elastically at that range of temperature. When under shear strain rates on the order of 0.1–1 s^{-1}, gelatin is a suitable analog for modeling viscoelastic responses such as seismic activity and fracture propagation within the Earth (van Otterloo and Cruden 2016).

Knowledge of the effective viscosity alone is not sufficient to describe the rheological properties of polymers and related materials (ten Grotenhuis et al. 2002). For that reason, gelatin rheology has been studied and documented in order to evaluate its suitability as a rock analog. Di Giuseppe et al. (2009), Kavanagh et al. (2013), and van Otterloo and Cruden (2016) are among those who researched the suitability of gelatin as a crustal and lithospheric analogue. They performed rheological analyses of its viscous and elastic attributes.

Recently, Kobchenko et al. (2013, 2014) studied fracture network evolution using gelatin and the yeast-mediated fermentation of sugar to produce CO_2 as an internal gas generation source. In their work, Kobchenko et al. (2013) placed a mixture of water, gelatin, sugar, and yeast in pre-determined proportions into a back-lit glass Hele-Shaw cell to visualize internal gas generation and fracturing. Once the gas generation prompted by the sugar fermentation starts, the increase in pressure and the rheological properties of the gelatin at the experimental conditions combine into the onset and growth of a fracture network that is optically and dynamically recorded with a camera for post-processing using image analysis. The open boundaries of the Hele-Shaw cell allow for the gas to escape from the matrix once the fracture(s) that carries it reaches the edge of the gelatin-occupied area. In these experiments, Kobchenko et al. (2014) observed fracture network evolution in order to study the dynamics of fracture patterns formed in a low-permeability elastic solid during internal fluid production and subsequent expulsion.

This paper presents a combined fine-scale mechanistic modeling and experimental campaign to improve physical understanding of the interplay of internal gas generation, solid deformation, and fracture network creation in viscoelastic solids. On the numerical modeling side, our problem involves the coupling of appropriate physics on multiple scales. In the most basic sense, we have (1) solid mechanical deformation, (2) fracture propagation, and (3) fluid flow in porous media and developed cracks. Specific to the phase-field fracture model, the coupling of solid deformation and fracture propagation can be done sequentially in a staggered update where the phase-field variable is updated first and then the displacement field is computed (Miehe et al. 2010b). Alternately, they can be coupled in a monolithic way using a primal–dual-active set strategy (Heister et al. 2015). Novel features of our approach include: accurate transformation of pressurized surface traction into smeared body force, stabilized equal-order displacement and pressure coupling, and conservative fluid mass during fracture propagation.

On the experimental side, we built a system similar to that described by Kobchenko et al. (2013) and performed a series of ordinary light (OL) imaging and polarized light (PL) imaging experiments. Importantly, we study response dependency with geomechanical parameters, such as Young's modulus. We used a range of laboratory-grade gelatin samples with variable gelatin strength in the experiments to observe and compare fracture network development correlation to Young's modulus. Phenomena are imaged at a length scale and time resolution not currently available to other imaging techniques such as X-ray computed tomography (e.g., Glatz et al. 2016, 2018). We employed image analysis to explore new trends and correlations among the measured variables on the experimental data set. We employed concepts from linear elastic fracture mechanics (LEFM) to explore novel perspectives on the measured

parameters and correlations among parameters that enhance the understanding of fracture net-work behavior as observed in the analog material. Measurements include gelatin permeability, length of fractures, distribution of fracture lengths, growth velocity, pressure at the fracture tip, as well as nucleation and coalescence events including the angle of coalescence. In PL experiments, we used photoelasticity imaging techniques to explore transient stress field responses in the crack propagation process and to develop a method to transform the imaging-derived data into quantitative stress field information, such as principal stresses around the crack tips and coalescence (fracture merging) nodes.

The novelty of our work is that microfracture networks are imaged and modeled as they form rather than measured after the fact. Host rock elastic-brittle fracture and fracture network propagation mechanisms are triggered by internal gas generation, microfracture frequency, connectivity, and topology are linked to material properties in a direct fashion. This paper proceeds with a discussion of relevant linear elastic fracture mechanics (LEFM), our computational and experimental frameworks, and then results.

2 Linear Elastic Fracture Mechanics

One of the most widely used criteria for fracture propagation is LEFM theory, developed by Griffith to explain the failure of brittle materials (Griffith 1921). It predicts that a fracture propagates if the release rate of strain energy with respect to incremental fracture length ∂_l is equal to critical energy release rate. The criterion can be interpreted as fracture surface energy creation in brittle fractures or combined with plastic dissipation in quasi-brittle fractures. In this section, we introduce the experimental and modeling approaches that we follow in supporting and developing our investigation. Figure 1 illustrates (a) the LEFM theory postulate, 1(b) a schematic of our setup for the experimental approach for monitoring the evolution of fractures and fracture networks, 1(c) a sample fractured region from our experimental results, and 1(d) the phase-field modeling approach.
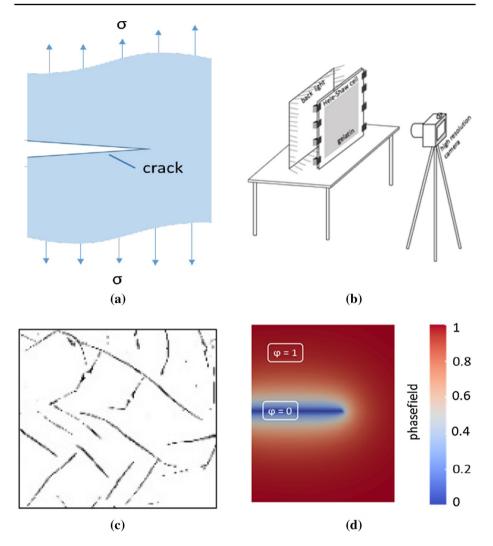
2.1 LEFM Experimental Approach: Analog Systems

LEFM principles have been used to describe dyke propagation (magmatic intrusion) and, importantly, have significant similarity with the gas-driven fracturing of source rocks. In both cases, a fluid of lower density intrudes the host matrix and dissipates energy, due to the increase in pressure, by fracturing the rock. We adopt those principles as applicable to this system. With similar assumptions, Kavanagh et al. (2006) propose a balance of pressures necessary to achieve intrusion and propagation. The intrusion pressure of the fluid needs to be equal to or greater than the hosting material's (gelatin) elastic pressure, P_e

$$P_e = \frac{E_m}{2\left(1 - v^2\right)} \frac{w_f}{y} \tag{1}$$

where E_m is Young's modulus, v^2 is Poisson's ratio squared, and w_f and y are the half thickness and half second smallest dimension of the initial crack. The ratio w_f/y is typically less than 1 in order to apply Eq. (1). Once the crack has nucleated, and in order to propagate, the pressure at the tip of the crack must exceed the strength of the host matrix. Fracture toughness, K_c, is a parameter defined to describe such strength as

$$K_c = \sqrt{2\gamma_s E_m} \tag{2}$$

Fig. 1 Investigation of stress field and fracture development in analogs for shale maturation: **a** schematic representation of the stress in linear elastic fracture mechanics (LEFM) theory as a pressurized crack grows, **b** setup for real time imaging of fracture nucleation and growth, **c** sample section of observed fractures in the gelatin matrix, and **d** phase field numerical approaches for simulating fracture growth

where Υ_s is the surface energy. The propagation pressure, P_p, is then expressed as

$$P_p = \frac{K_c}{\sqrt{\pi l}} \tag{3}$$

where l is the crack length. Assuming equilibrium, $P_e = P_p$.

2.1.1 Bloom Number and Young's Modulus

The working principle for measuring Bloom number is described in U.S. Patent No. 1,540,979 (Bloom 1925). It is similar to the Young's modulus measurement loading method presented by Timoshenko and Goodier (1970). The deflection caused by a load applied to the gelatin surface is measured and used in Eq. (4)

$$E_m = \frac{M_L g (1 - \vartheta^2)}{D_L d} \qquad (4)$$

where E_m is Young's modulus, ν^2 is Poisson's ratio squared, D_L is the diameter of the cylindrical load, M_L is its mass, d is the displacement caused, and g is the gravitational acceleration. The Bloom number is defined as the mass in grams necessary to indent a 12.5-mm diameter plunger 4 mm into a gelatin volume, and assuming the gelatin Poisson ratio value reported by Kavanagh et al. (2013) of 0.5, all parameters for Eq. (4) are defined, and calculation of Young's modulus via Bloom number is possible. Given that values for ν^2, D_L, and d are fixed (0.5^2, 12.5 mm, and 4 mm, respectively), Eq. (4) is rewritten as a function of Bloom number as

$$E_m = 147 \times \text{Bloom} \qquad (5)$$

Kavanagh et al. (2013) and van Otterloo and Cruden (2016) report Poisson's ratio (ν) values for gelatin of 0.5 and 0.451, respectively. Young's modulus (E_m) values are reported in Table 1 according to their Bloom number, as calculated by Eq. (5). Additionally, Kavanagh et al. (2013) report gelatin's surface energy (Υ_s) equal to 1 J m^{-2}. These are the values used in this work to calculate the parameters in Eqs. (2) and (3).

2.2 LEFM Modeling approach: Phase Field

In a continuum mechanics form, Griffith's criterion for fracture propagation is expressed as

$$\partial_l \left(\int_\Omega \frac{1}{2} \sigma(u) : e(u) dV \right) = \partial_l (G_c \Gamma) \qquad (6)$$

where σ is the stress tensor, that is a function of displacement u, and e is the infinitesimal strain tensor, G_c is the critical energy release rate, and Γ the surface area.

This original Griffith's criterion requires a preexisting crack and a pre-defined fracture path. Francfort and Marigo (1998) proposed another fracture propagation criterion that is able to predict the initiation of a fracture as well as fracture path:

Table 1 Gelatin Bloom number, calculated Young's modulus (E_m), calculated fracture toughness (K_c), measured permeability (K), diffusion coefficient (D), and stress-fringe factor (f_σ)

Bloom number	E_m (Pa)	K_c (Pa $\sqrt{m}$)	K (nD)	D (m^2/s)	f_σ (N/mm/fringe)
60	8820	132.81	1.56×10^{-2}	2.20×10^{-4}	0.016
100	14,700	171.46	1.54×10^{-2}	2.04×10^{-4}	0.025
250	36,750	271.11	2.16×10^{-3}	1.30×10^{-5}	0.035
300	44,100	296.98	1.11×10^{-3}	1.16×10^{-5}	0.043

$$\int_{\Omega \setminus \Gamma} \phi dV + \int_{\Gamma} G_c(\mathbf{x}) \cdot dH^{\dim - 1}(\mathbf{x}) \tag{7}$$

where $H^{\dim - 1}$ is the Hausdorff surface measure, ϕ is the strain energy density, Ω is the domain, and Γ is the surface area of the crack. The fracture propagation and path are found by taking the infimum of this energy functional. For numerical implementation, the energy functional is minimized at each time step with the constraint that the crack propagation is irreversible.

Following Biot's effective stress theory, the effective stress is expressed as $\sigma = \sigma_{total} + bp\mathbf{I}$, the energy functional Eq. (7) for a solid matrix is written as

$$E(u, C) = \int_{\Omega \setminus \Gamma} \frac{1}{2} \sigma(u) : e(u) dV - \int_{\partial_N \Omega} \tau u dS - \int_{\Omega} bp_M \nabla \cdot u dV + G_c \Gamma \tag{8}$$

where E is the energy of the system following Francfort and Marigo (1998), τ is the external force, and P_M the fluid pressure in porous matrix.

In the phase-field method, Γ is approximated as a Υ-convergent regularization of the discontinuity problem as suggested by Bourdin et al. (2000). More recently, it has been suggested (Tanné et al. 2018) that the following approximation is more suitable for crack nucleation:

$$\Gamma(\varphi) = \frac{3}{8} \int_{\Omega} \frac{(1 - \varphi)}{\varepsilon} + \varepsilon |\nabla \varphi|^2 dV \tag{9}$$

where φ is a scalar phase-field variable with $\varphi = 1$ indicating intact material and $\varphi = 0$ indicating broken material. Miehe et al. (2010a) argued that when minimizing the functional from Ambrosio and Tortorelli (1990) in phase-field model, the resulting partial differential equation for φ is diffusion-like with the property that when the length scale parameter ε tends to zero, the solution of φ approximates a discrete crack. The PDE of φ (Miehe et al. 2010a) is expressed as

$$\frac{G_c}{\varepsilon}(\varphi - \varepsilon^2 \Delta \varphi) = 2(1 - \varphi)\phi(u) \tag{10}$$

In the following section, we develop a phase-field representation of our system.

3 Numerical Modeling Theoretical Framework

3.1 Graphical Interpretation of Phase-Field Functional

The phase-field variable can be interpreted as an indicator function for the fracture and solid matrix. If we calculate the homogeneous solution to Eq. (10) with Dirichlet boundary condition $\varphi = 1$ on a straight line, the result converges to a discrete crack as $\varepsilon \to 0$, as illustrated in Fig. 2. Following the same form of regularized strain energy from (Bourdin et al. 2000) and also applying the quadratic degradation to Biot pressure coupling, we then plug Eq. (9), the approximation to the crack surface, into the energy functional Eq. (8) to obtain

$$E(u, \varphi) = \int_{\Omega} \frac{1}{2} \varphi^2 \sigma(u) : e(u) dV - \int_{\partial_N \Omega} \tau u dS - \int_{\Omega} b\varphi^2 p_M \nabla \cdot u dV + G_c \Gamma$$
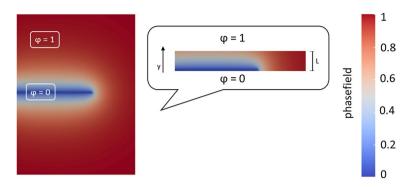$$+ \frac{3}{8} G_c \int_{\Omega} \frac{(1 - \varphi)}{\varepsilon} + \varepsilon |\nabla \varphi|^2 dV \tag{11}$$

Fig. 2 Phase-field crack approximation in 2D, with fracture half-length L. Note the continuous variation of phase field variable, φ

In Eq. (11), the traction boundary condition is written as $\int_{\partial_N \Omega} \tau u dS$ and needs special consideration. First, notice that the traction force comes from two sources: (1) traction acting on existing solid matrix boundaries and (2) fluid pressure acting on newly created fracture surfaces. While the former can be simply denoted as $\int_{\partial_M \Omega} \tau u dS$ without further modification, there are complications for the second traction force.

3.2 Fracture Interface Law

The boundary condition between fracture and solid matrix should converge to a discrete crack when $\epsilon \rightarrow 0$. For a discrete crack, two conditions have to be satisfied, as follows.

1. Force balance: at the intact region ($\varphi = 1$) surrounding the fracture, the normal stress perpendicular to the fracture surface should equal to the pressure at the fractured region ($\varphi = 0$) and this is written as $(\sigma - b p_M I) \cdot n|_M = -p_f n|_F$.
2. Conservation of fluid mass is written as $\frac{\partial \rho V_{\text{fluid}}}{\partial t}\Big|_M + \frac{\partial \rho V_{\text{fluid}}}{\partial t}\Big|_F = 0$.

The second condition is automatically satisfied in the continuum formulation developed in the next section. To satisfy the first equation, we proceed in the surface integral form:

$$
\begin{aligned}
\int_{\partial_F \Omega} \tau \cdot u dS &= \int_{\partial_F \Omega} (-p_F I) n \cdot u dS \\
&= \int_{\partial_F \Omega} (-(1 - \varphi) p_F I) n \cdot u dS
\end{aligned}
\tag{12}
$$

Note that at fracture surfaces, the phase-field variable is equal to 0 and, therefore, multiplying the original equation by $(1 - \varphi)$ does not change the result. The reason why we multiply by the continuous function $(1 - \varphi)$ is to transform easily into a volume integral that satisfies the traction boundary condition. Because in the phase-field model there is not a discrete fracture boundary, such as $\partial_F \Omega$, all the balance laws should be written in a volume integral form. More precisely, the traction energy $\int_{\partial_F \Omega} \tau u \cdot dS$ needs to be converted into a

volume integral with inaccuracy controlled in a thin region that vanishes as $\epsilon \to 0$, as illustrated in Fig. 2.

By considering the following volume integral, this requirement is satisfied as

$$
\int_{\partial_F \Omega} \int_L \frac{\partial}{\partial y}((1-\varphi)p_F \mathbf{I})n \cdot u \, dy dS
$$
$$
= \int_{\partial_F \Omega} (-(1-\varphi)p_F \mathbf{I})n \cdot u|_{\varphi=1}^{\varphi=0} dS \tag{13}
$$
$$
= \int_{\partial_F \Omega} (-(1-\varphi)p_F \mathbf{I})n \cdot u dS
$$

which is exactly equal to Eq. (12). Following the approximation to a fracture surface normal proposed in Mauthe and Miehe (2017), the normal is approximated as $n = \frac{\nabla \varphi}{|\nabla \varphi|}$. Therefore, the volume integral is written as

$$
\int_{\partial_F \Omega} \int_L \frac{\partial}{\partial y}((1-\varphi)p_F \mathbf{I})n \cdot u \, dy dS
$$
$$
= \int_{\Omega} -\nabla[(1-\varphi)p_F \mathbf{I}]n(n \cdot u) dV \tag{14}
$$
$$
= \int_{\Omega} -\nabla[(1-\varphi)p_F \mathbf{I}]n \otimes n \cdot u dV
$$

We compare our strategy with that described in Lee et al. (2016). Our model has the property that the approximation is controlled in a small region around the fracture with width governed by length-scale factor ϵ. Also, the Biot coefficient term in the energy functional $\int_{\Omega} -b\varphi^2 p_M \nabla \cdot u dV$ will remain intact within porous media.

The modified energy functional then becomes

$$
E(u, \varphi) = \int_{\Omega} \frac{1}{2}\varphi^2 \sigma(u) : e(u) dV - \int_{\partial_M \Omega} \tau u dS - \int_{\Omega} b\varphi^2 p_M \nabla \cdot u dV
$$
$$
+ \int_{\Omega} \nabla[(1-\varphi)p\mathbf{I}]n \otimes n \cdot u dV + \frac{3}{8}G_c \int_{\Omega} \frac{(1-\varphi)}{\epsilon} + \epsilon|\nabla \varphi|^2 dV \tag{15}
$$

3.3 Fluid Mass Balance Equation

We chose to use fully implicit coupling between solid displacement and fluid pressure because of the unconditional time step stability and the superior convergence rate of Krylov solvers. Importantly, we use a fixed-stress preconditioning strategy with algebric multigrid inner preconditioner to solve the linear system using BiCGstab (White et al. 2016). Because the phase-field variable varies smoothly from 0 to 1, it is used as an indicator function for fracture versus matrix. To proceed, we use the Darcy's flow approximation of Lee et al. (2016).

In the following, we use subscript M to denote that the quantity is within the porous matrix, and subscript F denotes that the quantity is within the fracture. Then, the fluid conservation in porous media is

$$\rho \partial_t \left(\frac{1}{M} p + b \nabla \cdot u \right) - \nabla \cdot \frac{\mathbf{k_M} \rho}{\eta} (\nabla p - \rho g) = q \tag{16}$$

and within the fracture

$$\rho \partial_t (cp) - \nabla \cdot \frac{\mathbf{k_F} \rho}{\eta} (\nabla p - \rho g) = q \tag{17}$$

where $k_F = k_M \mathbf{I} + \frac{w^2}{12} m \otimes m$ according to the Poiseuille-type fluid flow, and the fracture aperture, w, is estimated from local deformation (Mauthe and Miehe 2017). The fracture direction unit vector m is normal to $n = \frac{\nabla \varphi}{|\nabla \varphi|}$, M is the Biot modulus, and μ is the dynamic viscosity of the fluid. A simple combination by taking the phase-field variable φ as an indicator function, i.e., Equation (16)$\times \varphi +$ Eq. (17)$\times (1 - \varphi)$, does not conserve fluid mass. Therefore, we introduce a conservative formulation as follows.

Because a naive convex combination of these two equations does not yield a conservative fluid mass, we need to define a mass storage function that itself depends on the phase-field variable. Our choice of fluid mass storage function per unit volume is expressed as

$$m = \varphi(\rho_F \phi) + (1 - \varphi)\rho_F \tag{18}$$

With the conditions $\rho_F \approx \rho_0 \left(1 + c_F (p - p_0) \right)$, and $\rho_F \phi \approx \rho_0 (\phi_0 + \frac{1}{M}(p - p_0) + b(\nabla \cdot u - \varepsilon_{v,0})$, where the Biot modulus is $\frac{1}{M} = \frac{(b - \phi_0)}{K_s} + \phi c_F$, and taking the derivative of Eq. (15) with respect to time

$$\frac{\partial m}{\partial t} = \varphi \rho_0 \left[\frac{1}{M} \frac{\partial p}{\partial t} + b \frac{\partial}{\partial t} (\nabla \cdot u) \right] + (1 - \varphi) \rho_0 c_F \frac{\partial p}{\partial t} + \frac{\partial \varphi}{\partial t} (\rho_F \phi - \rho_F) \tag{19}$$

then the fluid conservation equation becomes

$$\partial_t(m) - \nabla \cdot \frac{\rho}{\eta} \left[\varphi \mathbf{k_M} + (1 - \varphi) \mathbf{k_F} \right] (\nabla p - \rho g) = \rho q. \tag{20}$$

3.4 Bilinear Form

The weak form is derived from the energy functional. But first, the stress is decomposed into its compression and extension components, following the procedure described in Amor et al. (2009), as

$$E(u, \varphi) = \int_\Omega \frac{1}{2} [\varphi^2 \sigma^+(u) : e(u) + \sigma^-(u) : e(u)] dV - \int_{\partial_M \Omega} \tau u dS - \int_\Omega b\varphi^2 p_M \nabla \cdot u dV$$
$$+ \int_\Omega \nabla[(1 - \varphi)p\mathbf{I}] n \otimes n \cdot u dV + \frac{3}{8} G_c \int_\Omega \frac{(1 - \varphi)}{\varepsilon} + \varepsilon |\nabla \varphi|^2 dV$$

$$\tag{21}$$

In order to simplify implementation, we assume the pressure gradient and fracture surface normal are approximately in the same direction, in which case the $n \otimes n$ term can be neglected. Then, the weak form is

$$\delta_u E = \big(\big((1-k)\varphi^2 + k \big) \sigma^+(u), e(w) \big) + (\sigma^-(u), e(w))$$
$$- b(\varphi^2 p, \nabla \cdot w) - p\nabla\varphi \cdot w + (1-\varphi)\nabla p \cdot w \quad (22)$$

The balance of the linear momentum equation with degradation of strain energy is

$$\delta_\varphi E = (1-k)(\varphi\sigma^+(u) : e(u), \psi) - 2b(\varphi p \nabla \cdot u, \psi) - p\nabla\psi \cdot u$$
$$- \psi\nabla p \cdot u + \frac{3}{8}G_c\left(\left(\frac{1}{\varepsilon}, \psi\right) + 2\varepsilon(\nabla\varphi, \nabla\psi)\right) \quad (23)$$

This is a diffusion-like equation with $\varphi\sigma^+(u): e(u)$ acting as a source term. One of the strategies to impose the irreversibility condition $\partial_t <= 0$ is to set this source term as a history-maximum (Miehe et al. 2010b).

The Jacobian of the weak form is found by taking the second variation of $\delta^2 E$ as

$$\delta\delta_u E = \big(\big((1-k)\varphi^2 + k \big) \sigma^+(\delta u), e(w) \big) + (\sigma^-(\delta u), e(w))$$
$$+ (2(1-k)\delta\varphi\sigma^+(u), e(w)) - 2b(\delta\varphi p, \nabla \cdot w) - p\nabla\delta\varphi \cdot w + \delta\varphi\nabla p \cdot w \quad (24)$$

and

$$\delta\delta_\varphi E = (1-k)(\delta\varphi\sigma^+(u) : e(u), \psi) - 2b(\delta\varphi p \nabla \cdot u, \psi) - p\nabla\psi \cdot \delta u$$
$$- \psi\nabla p \cdot \delta u + \frac{3}{8}G_c(\nabla\delta\varphi, \nabla\psi). \quad (25)$$

3.5 Solution Structure

Originally, a monolithically coupled system is expressed as

$$\begin{bmatrix} M^{uu} & M^{u\varphi} & M^{up} \\ M^{\varphi u} & M^{\varphi\varphi} & M^{\varphi p} \\ M^{pu} & M^{p\varphi} & M^{pp} \end{bmatrix} \begin{Bmatrix} u \\ \varphi \\ p \end{Bmatrix} = \{\text{Residual}\} \quad (26)$$

We divide the full system of equations into two smaller systems. The solid displacement and fluid pressure are implicitly coupled because of the unconditional time step stability and superior convergence rate of Krylov solvers. For this system of equations, we use a fixed-stress preconditioning strategy with Algebric Multigrid inner preconditioner to solve the linear system with BiCGstab (White et al. 2016). This system is coupled with a phase-field equation in a sequential iterative manner and looped until convergence (Bourdin et al. 2000).

$$\begin{bmatrix} M_{uu} & M_{up} \\ M_{pu} & M_{pp} \end{bmatrix} \begin{Bmatrix} \Delta u \\ \Delta p \end{Bmatrix} = \begin{Bmatrix} R_{\text{momen}} \\ R_{\text{mass}} \end{Bmatrix} \quad \text{and} \quad [M_{\varphi\varphi}]\{\Delta\varphi\} = \{R_{\text{phase}}\} \quad (27)$$

Our simulation code was written in C++ and linked against the DEAL.II finite element library (Bangerth et al. 2007). We incorporated some modules from the open-source phase-field simulation code by Heister et al. (2015) that only takes into account the solid deformation. The phase-field irreversibility constraint is maintained by a switch between primal–dual-active-set approach (Hintermüller et al. 2002) and history-maximum-source term approach (Miehe et al. 2010a, b).

3.6 Stabilized Low-Order Interpolation for Solid/Fluid Coupling

It is well known to the mixed-finite element community that the kind of coupling between solid/fluid used here sometimes causes numerical stability issues (Bochev et al. 2006). Specifically, if we have a nearly incompressible fluid and incompressible rock, and the permeability is low, as is the case for shale, a stability problem may arise. Therefore, we have to choose the spaces for displacement S_u^h and pressure S_p^h such that they satisfy the discrete Ladyzenskaja–Babuška–Brezzi (LBB) condition

$$\sup_{v^h \in S_u^h} \frac{\int_\Omega q^h \nabla \cdot v^h \mathrm{d}\Omega}{\left\| v^h \right\|_1} \geq C \left\| q^h \right\|, \quad \forall q^h \in S_p^h \tag{28}$$

Following the polynomial-pressure-projection technique that was introduced into the poro-mechanics community by White and Borja (2008), we add a stabilization term in the mass conservation equation for the fluid

$$H_{\text{stab}}^{n+1} = \int_\Omega \frac{\tau}{2G\Delta t}(\psi^h - \Pi\psi^h)(p^{n+1} - \Pi p^{n+1} - p^n + \Pi p^n)\mathrm{d}\Omega \tag{29}$$

If we use first-order interpolation for displacement and pressure, we can apply a constant projection onto a piecewise constant interpolator

$$\Pi p^h|_{\Omega^e} = \frac{1}{V^e} \int_\Omega p^h \mathrm{d}\Omega \tag{30}$$

By doing this, we are able to recover the stable solution even in the undrained limit.

4 Experimental

A systematic experimental structure was created in order to serve as benchmarking data for the numerical model. Gelatin was utilized as a rock analog to create a reacting solid that evolves a separate phase similar to kerogen maturation in shale.

The experimental setup consists of a vertical Hele-Shaw cell, held by clamps, filled with a mixture of water, laboratory-grade gelatin, white sugar, and active dry yeast in predetermined proportions, and set to gel (Fig. 3a). The proportions are based on the specifications reported by Kobchenko et al. (2013): 7.5 g of sugar, 2.5 g of yeast, and 58 g of gelatin per 1000 cm^3 of water. In this work, for ordinary light (OL) imaging experiments, a 5.5 wt% gelatin solution was used, while the polarized light (PL) imaging or photoelasticity imaging tests were prepared with 6.7 wt% gelatin solution, in order to match Bloom number test standards. The glass plates that make up the Hele-Shaw cell have dimensions

of 25.4×25.4 cm and are 1 cm thick. The edges of the cell are not confined because the perimeter serving as a drainage zone. The glass plates are separated by 2 mm of gelatin film.

The glass plates are carefully cleaned, primed with hydrophilic fluids, and stored in a distilled water bath in order to favor adhesion of the gel to the glass walls. Once the gelatin is prepared and homogenously mixed, half the prepared volume is poured into the Hele-Shaw cell and the other half is poured into a plastic bottle that is connected to a gas volume measuring setup (Fig. 3b). The gas volume production measurement step is skipped in the photoelasticity tests. Assuming homogenous distribution of the yeast in the gelatin solution, the volume of gas produced in the Hele-Shaw cell is assumed to be equal to the volume of gas measured in the volumetric system. Both Hele-Shaw cell and plastic bottle are placed inside a refrigerator at 1 °C. There, the cell is oriented vertically for around 2 h and then tilted 90° in order to ensure proper gelation and glass wall adhesion.

The experiment is started by removing the cell and bottle from the refrigerator and placing them in the imaging setup. The imaging setup consists of a flat horizontal surface where a pair of supporting clamps holds the Hele-Shaw cell vertically against a white LED backlight source. The plastic bottle is connected to the volumetric measuring system. Images are recorded using a high-resolution camera (Canon EOS7 with 18 MP image resolution, resulting in an average spatial resolution of 165 μm/px) with image acquisition every 1 min. Readings from the volumetric system attached to the plastic bottle are collected periodically. The experiments are recorded for a period varying between 22 and 24 h (Fig. 3).

When subject to a large amount of stress in a relatively short period of time, gelatin tends to display elastic behavior, while smaller amounts of stress, applied for a longer period of time are responded to viscously (Di Giuseppe et al. 2009). Therefore, it is important to select carefully experimental conditions that favor the elastic/brittle behavior that is required to induce fracture network generation and growth. The imaging area is kept at an average of 14±1 °C, in order to maintain elastic behavior of the gelatin. Figure 3 illustrates (a) the setup at the imaging area, (b) gas volume measuring system, and (c) permeability test apparatus based on the description provided by Brace et al. (1968). Four OL tests (OL-60, OL-100, OL-250, and OL-300 for Bloom 60, 100, 250, and 300, respectively), and four photoelastic or PL tests (PL-60, PL-100, PL-250, and PL-300 for Bloom 60, 100, 250, and 300, respectively) are reported here.
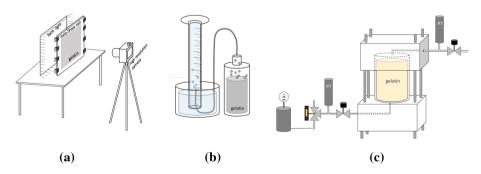

(a)   **(b)**   **(c)**

Fig. 3 Experimental apparatus for ordinary light tests at the imaging area **a** imaging setup and **b** volumetric measurement setup, **c** permeability measurement apparatus

4.1 Gelatin Properties

4.1.1 Permeability

Gelatin permeability (unfractured) was estimated utilizing the experimental principles described by Brace et al. (1968), otherwise known as pulse-decay tests. A polycarbonate apparatus with a no-confining pressure coreholder of 1.25 cm. diameter was used to measure the transitional response of a pulse of gaseous pressure over a casted-on gelatin cylinder. The gas used was CO_2 because it corresponds to the gas produced by yeast. Samples of gelatin of Blooms 60 to 300 were tested. Permeability was then calculated as

$$K_d = \frac{\alpha_d \mu \beta L}{A \left(\frac{1}{V_1} + \frac{1}{V_2} \right)} \tag{31}$$

where K_d is permeability, α_d is the slope of the semilog curve $P_1 - P_f$ versus time, μ is the gas viscosity, β is the gas compressibility, L is the length of the gelatin core, A is the cross-sectional area, and V_1 and V_2 are the dead volumes at the inlet and outlet of the apparatus, respectively.

4.1.2 Diffusion

Gelatin diffusion is estimated from permeability measurements as described above. Arvanitoyannis et al. (1997) and Charmette et al. (2004) used pressure decay data to calculate gelatin diffusion by approximating Fick's second law to steady state

$$D = \frac{L^2}{6\theta_{ss}} \tag{32}$$

where D is the diffusion coefficient and θ_{ss} is the time at which steady state is reached.

4.2 Photoelasticity

Photoelasticity is a nondestructive, whole-field, graphic stress analysis technique employed in diverse 2D and 3D applications to infer experimentally stress fields in solids. It is based on an optomechanical property called birefringence exhibited by some transparent materials and is primarily used for analyzing two-dimensional problems, although it is applicable to 3D cases mainly by the use of birefringent coating materials (Phillips 2008). Birefringent materials exhibit dual refraction indices such that when a ray of light passes through them, it splits into two rays that take different paths and different speeds, often referred to as phase retardation. Several crystals and other transparent materials, such as polymers and gelatins, exhibit one form or another of birefringence. In photoelastic materials, birefringence is such that when a ray of light passes through, it gets resolved along the two principal stress directions that correspond with its two different refractive indices (Li 2010). In 1853, Maxwell reported that the refractive indices were linearly proportional to the loads of an elastic material and expressed the relationship through the stress optics law. It is often written in terms of the number of complete retardation cycles (or fringe order) and fringe constant, expressed as

$$\frac{Nf_\sigma}{h} = \sigma_1 - \sigma_2 \qquad (33)$$

where N is the fringe order, h is the thickness of the gelatin element, f_σ is the material stress-fringe factor, and σ_i are the principal stresses. Fringes are optical effects produced as a consequence of the optical interference of the two waves caused by the dual refraction indices. They appear as a series of successive and contiguous bands that represent a different degree of birefringence corresponding to the underlying strain in the sample. Fringes will appear first at the most highly stressed points. As the stress field changes, as it does in the case of crack propagation, the initial fringes are pushed toward the areas of lower stress and ultimately moved toward regions of zero or low stress until the maximum load is reached (Vishay Group 2011). The sequence in which the fringes appear determines the fringe order. Then, according to Eq. (33), it follows that the difference in the principal stresses is obtained by calculating the fringe order and multiplying by the material fringe constant.

The method of photoelasticity is based in the identification of fringes and fringe order and requires the use of polarizing filters. Polarizers convert randomly polarized light into plane-polarized light, acting like a filter of light propagation direction, allowing passage only of those waves that are parallel to the polarizer direction. A plane polariscope consists of a light source, a polarizer, the sample to be studied, and an analyzer. An analyzer is also a polarizing filter, but rotated to have the polarizing direction normal to the polarizer. The optical principles and functional description of the polariscope are well described in the literature (Anderson 1978; Phillips 2008; Ramesh 2000; Li 2010; Baek et al. 2014; and Ju et al. 2017) and are not the focus of this work.

The stress-fringe factor of a material is estimated with a calibration loading experiment where a sample disk made of the tested material is loaded diametrically and imaged with white polarized light. Colored bands appear on the image as a product of the attenuation and extinction of one or more colors from the white spectrum, and the sequence of colors is produced by an increasing stress field (Dally and Riley 1991). The fringe order, N, is estimated using the isochromatic band approach, where direct visual observation of the band color is cross-referenced to a table indicating fractional fringe order (up to a fringe order of approximately 4). For a diametrically loaded disk, the stress-fringe factor f_σ, is determined by

$$f_\sigma = \frac{8P}{\pi DN} \qquad (34)$$

where P is the load applied to the disk, D is its diameter, and N is the fringe order. A gelatin disk of similar weight concentration as that used in the fracture network experiments was created for each gelatin strength (Blooms 60, 100, 250, and 300). The disks were diametrically loaded and imaged with white polarized light. A color sequence and fringe order table (Dally and Riley 1991) was used to determine fringe orders, and Eq. (34) was used to calculate the corresponding stress-fringe factors.

Table 1 shows calculated Young's modulus, fracture toughness, permeability, diffusion coefficient, and stress-fringe factor for the Bloom numbers of the gelatins used in this study. The values reported seem to cluster gelatin samples into two groups: low Bloom (60 and 100) and high Bloom (250 and 300), because the values within these subsets are relatively close, suggesting nonlinearity in rheological behavior respective to Bloom number.

4.3 Image Analysis

Each experiment produced a set of still images that illustrates the evolution of the gas self-generating system and the resulting fracture network with time. The image analysis code that was developed in MATLAB and its GUIDE toolbox to process the acquired data includes a user interface that allows for fine tuning and logging of the pre-processing parameter values chosen for each data set. Pre-processing parameters include image cropping, masking, and thresholding. Because the computational expense is too large to process all of the images, a function that selects a user-capped subset of images with the largest changes respective to the previous images is included on the interface.

The pre-process analysis has the following sequence. A source folder, where all acquired images are contained, is selected. The user is shown the last image as a visual reference for cropping and converting from RGB to grayscale to black and white (binary). A binary thresholding level is then manually selected by the user to correct for backlight intensity variations. Image selection follows where the initial image from time$=0$ is subtracted from each binary image subset at time$=t$ in order to normalize all images to the initial background. By calculating successive changes between one image and the next, those with the largest absolute change are shortlisted for a final pick of a maximum number of images set by the user. This maximum number is often close to 120 images in order to be computationally viable.

Nucleation sites are defined as the location where the fracture first appears. At the time of nucleation, a consecutive identification number or ID is assigned to the new fracture, and it is preserved for the duration of the analysis. Fracture nodes are defined as the location(s) at which a pair of fractures connects with each other. These nodes are user-identified on the image on which they occur and their coordinates recorded in order to identify fracture connection events. The elastic behavior of the system and fluctuations of the gas pressure cause opening and closing of the fractures. In order to track all fractures occurring at any time in a given location, a new set of binary cumulative fracture images is created from the original image subset. For each image at time$=t$, each new individual fracture is identified and labeled, while previously existing fractures are tracked in order to follow their evolution.

Once the pre-processing functions have been completed, all morphological features represented in the images are calculated as they change with time.

5 Results and Discussion

Numerical and experimental results are now presented. Test cases are developed with nucleation sites that are treated as fracture originating defects that develop into elliptical voids with a range of diameters. Next, a sample fracturing process run with experimentally valid parameters is shown and discussed. For the experimental results, an array of plots are displayed to illustrate the relevance of the gelatin strength on the fracture system behavior and development for the OL experiments, followed by a similar array showing examples of stress-induced light intensity maps for each gelatin strength used in the experiments at different stages of fracture network development. Finally, a side-by-side comparison of some of the numerical and experimental results is presented in order to corroborate the degree of agreement achieved.
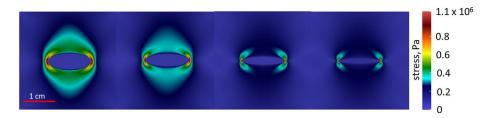
Fig. 4 Numerical results: Stress distribution for elliptical voids with decreasing aspect ratios of 0.4, 0.3, 0.2, and 0.1, from left to right

5.1 Stress Distribution Around Elliptical Void

By studying the stress distribution, we get a better sense of the nucleation mechanism of the fractures. As a first hypothesis, we assume the defect in the gelatin has an elliptical shape. When the pressure builds up within the sample, the concentrated stress around the fracture tip elongates the defect and eventually becomes a propagating thin crack.

To verify this hypothesis, four models were generated, all of them have an elliptical inclusion but with different aspect ratio as shown in Fig. 4. For a small aspect ratio and circle-like inclusion, the stress distributes evenly around the defect. When the aspect ratio is greater, the stress mostly concentrates on the fracture tip and with greater magnitude bends toward the fracture. This finding coincides with the experimental results (to be described later in this section), and it could be a mechanism behind the nucleation process for a single fracture.

5.2 Fracture Network Prediction Based on Images

Ideally, we wish to predict the evolution of the fracture network without any a priori knowledge about the nucleation site of the fracture. This requires either (1) certain statistical information about the distribution of defects and sources in the sample or (2) knowledge of the exact spatial heterogeneity in the sample. An alternative approach consists of populating the defect distribution directly from experimental images acquired at the time of nucleation. Numerical simulation is then performed to observe the growth pattern of
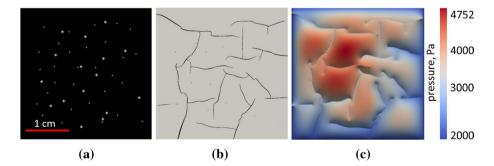

(a)　　　　　　　　(b)　　　　　　　　(c)

Fig. 5 Numerical results: **a** initial seeds of defects, **b** resulting fracture network, **c** pressure distribution within matrix and fractures

fractures. In the test results shown in Fig. 5, Young's modulus is set to 1.0×10^4 Pa, the critical energy release rate is 1.0 J/m^2, and gas generation in the entire domain is uniform with a gas production rate of 0.04 cm^3/min.

Figure 5a shows the initial distribution of defects (in white) on the matrix. Figure 5b shows that the resulting fractures maintain some distance from each other and stop after finding a drainage path to the boundary. In most cases, the greater the aspect ratio, the more likely it is that the defect propagates. If the defect is too close to the drainage boundary, it tends to not propagate even if it has a large aspect ratio. Pressure tends to be larger toward the center of the matrix and consistently decrease toward the drainage boundaries, as shown in Fig. 5c.

5.3 Experimental Tests General Considerations

5.3.1 System Behavior

Once the Hele-Shaw cell is placed in the imaging area, it takes an average of 3 h for the gas produced by the yeast-driven sugar fermentation process to nucleate fractures. In early stages, fractures propagate from one or both ends until they reach an edge of the gelatin matrix and/or merge with another fracture. As the process develops, fractures exhibit elastic behavior in that they intermittently open and close in accordance with the rate and pattern of gas produced as a by-product of the sugar fermentation. At later times, some of the fractures completely close as the gas production in their location declines.

5.3.2 Image Analysis and Parameters

Once the image is binarized, the image analysis code identifies and tracks each of the fractures that are generated and propagated in the network. A fracture network map is created based on the image analysis and fracture tracking performed by assigning successive, increasing fracture ID numbers to each fracture. The fracture ID numbers are also indicators of the order of appearance, such that smaller ID numbers correspond to early fractures and larger ID numbers correspond to late-nucleated ones. Fracture length is recorded with time for every individual fracture and total fractured length bases, and is reported as final fracture length distribution and cumulative fracture length.

Nucleation site locations for each fracture that developed are identified and mapped in the gelatin matrix space. Time of location is indicated via a color map. Morphology of the fracture network is tracked as it pertains to length, maximum growth speed, order of appearance, and number of connections by way of a scatter chart, color map, and data point marker size, respectively. Fracture nucleation and merging events are charted together versus time (proxy by image number) in order to explore trends in temporal fracture emergence and interaction. Angles of coalescence are calculated and normalized between 0 and 90 degrees to help assess fracture path deflection as a result of fracture interaction and its effect on the gelatin matrix stress field. Fracture path deflection is a function of the stress field in the host matrix that in turn is dependent on fracture growth stage and interaction among fractures. Watanabe et al. (2002) showed in their experiments that crack deflection may occur when the shear stress around a crack changes the orientation of a following crack from vertical to parallel to the maximum compressive stress, causing it to bend toward the preceding crack, as previously proposed by Takada (1994). The stress caused by a fracture, however, varies

over time. As the pressuring fluid builds up, the fracture is drained. Therefore, the merging angle depends on the stress field around the cracks at the time of the merge.

5.3.3 Ordinary Light (OL) Tests

As mentioned earlier, gelatin rheology plays a critical role in characterizing the crack propagation process because it dials its viscoelastic behavior toward one end or another of the spectrum. Gelatin with small strength has a greater viscous behavior component, while elastic behavior takes predominance as gelatin strength increases. In this work, laboratory-grade gelatin with measured Bloom number is used in order to establish a correlation between measurable parameters as described in the previous section and gelatin strength. This analysis is later translated to source rock geomechanical maturation behavior and correlated to its Young's modulus.

Four laboratory-grade gelatins were selected according to Bloom number to cover the 'low' to 'high' spectrum, as described by Sigma-Aldrich (2018). Selected Bloom numbers (in ascending gelatin strength) are 60, 100, 250, and 300. Their calculated Young's modulus according to Eq. (5) are shown in Table 1. Repeatability tests were conducted for each Bloom number to verify characteristic behavior for each gelatin. Selected experiments are referred to as OL-60, OL-100, OL-250, and OL-300 for Bloom numbers 60, 100, 250, and 300, respectively.

5.3.4 Fracture Network Morphology

Figure 61a shows the final fracture network map for OL tests including fracture ID numbers. OL-60 fracture network (Fig. 61a) reveals a densely fractured gelatin matrix that adds up to 900+ short and lineal fractures. OL-100 (Fig. 61b) shows a significant decrease in fracture density and an increase in fracture length compared to OL-60, exhibiting more fracture path deflection. Results for OL-250 (Fig. 61c) show an intermediate amount of fractures between that of OL-60 and OL-100, with straighter fracture paths than OL-100, while OL-300 (Fig. 61d) shows the smallest number of fractures with no fracture coalescence and no path deflection.

Results in Fig. 61a for OL-60 then may suggest that its gelatin K_c value is widely met by the gas pressure generated by yeast at a large number of locations in the gelatin matrix, making diffusion unnecessary for gas to transport itself and resulting in a large amount of almost evenly spaced fractures. Due to the large frequency of nucleation, significant fracture spatial density is achieved and nucleated fractures quickly collide with neighbors thereby limiting the extent of their growth and length. In the OL-100 case (Fig. 61b), the increase in K_c and only modest decrease in permeability and diffusion coefficient allow for more gas to diffuse inside the matrix before its pressure can reach the deformation threshold, while at some other sites, gas accumulates and breaks through, causing nucleation and further fracturing. Therefore, fewer nucleation sites are created and those that develop fractures are supported by diffused gas from other locations. This results in fracture growth in a larger available matrix area and longer fractures but with virtually no gas flow inhibition.

In the case of OL-250 gelatin (Fig. 61c), a significant increase in the K_c value along with a significant decrease in permeability and diffusion coefficient, as shown in Table 1, result in an increase of inhibited sites. Generated gas has difficulty flowing, thus creating less nucleation sites as compared to OL-60. There are more sites compared to OL-100
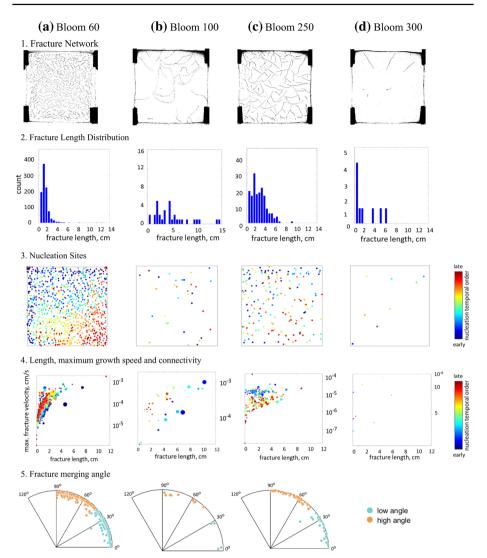
Fig. 6 OL tests for Blooms 60–300. 6.1. Cumulative fracture networks, 6.2. Fracture length distributions, 6.3. Nucleation sites, 6.4. Fracture length, growth and connectivity, 6.5. Fracture merging angle

perhaps due to less gas diffusion capacity to carry through the matrix that in turn favors clusters of local pressure accumulation that result in deformation. Fractures in OL-250 are shorter than those in OL-100 because they are less (or not) fed by neighboring diffusion and have less growth space availability before colliding with another fracture. Finally, OL-300 gelatin's K_c and the minimal permeability value surpass the capacity of the yeast system to generate enough gas to meet diffusion or deformation minimum requirements in most of the all sites, resulting in maximum inhibition and minimal fracturing (Fig. 61d).

Figure 62a–d provides insight into the fracture morphology for each test. OL-60 fracture length distribution (Fig. 62a) shows significant skew toward the left, with large counts of short fractures measuring less than 1 cm and the maximum length of a single fracture of

~4.5 cm. OL-100 distribution (Fig. 62b) shows a slightly more balanced length among the fractures, with most of them measuring less than 5 cm and maximum single fracture length of ~14 cm. The fracture length distribution for OL-250 (Fig. 62c) is again, skewed to the left, but with a flatter curve and similar counts for lengths between 0.5 and 3 cm, and a maximum single fracture length of 7 cm. Finally, OL-300 length distribution (Fig. 62d) spreads wider over the length range, with short fractures skewing the curve to the left. Notice some of these short fractures are little more than a freshly nucleated bubble, unable to overcome K_c.

Figure 63a–d shows nucleation site locations for each fracture developed in OL experiments. The blue tones in the color bar represent early-nucleated fractures, and the green and red tones represent those nucleated in middle and late stages of the process, respectively. Figure 63a shows that for test OL-60, early fractures (blue tones) tended to nucleate close to the upper left corner of the matrix, and as the network developed, nucleation sites migrated diagonally through the center (green-yellow tones), until late nucleation events clustered in the lower right corner. In Fig. 63b (OL-100), no trend of early, middle, or late nucleation sites is significantly observed, while in Fig. 63c (OL-250), the trend from OL-60 is loosely repeated. Finally, Fig. 63d (OL-300) shows all fractures tended to appear in the upper diagonal of the matrix, most of them near the edges. It is proposed that stress field dynamics on each test may be playing a role in the description of the nucleation sites distribution, but more investigation is required.

Figure 64a–d illustrates the morphology of the fracture network pertaining to the length, maximum speed reached, order of appearance, and number of connections of the fractures in OL experiments. The bubble size indicates the number of connections of the fracture and bubble color indicates timeframe of nucleation: early (blue shades), middle (green shades), or late (red shades). The x-axis correlates with the final fracture length and the y-axis with its maximum velocity.

Figure 64a shows that the short fractures that occurred in OL-60 tended to grow fast, relative to the maximum speed of the other samples, and most connected at least once with another fracture. Fractures in OL-100 (Fig. 64b) were, on average, the fastest growing fractures of the group and only about half of them coalesced with another fracture. Data in Fig. 64c show that while fractures tended to be medium sized, they were also slower growing than lower Bloom samples, OL-60 and OL-100, with a large ratio of connected fractures versus single ones. Finally, fractures in OL-300 (Fig. 64d) spanned the smallest to medium size length and showed the slowest growth and zero connectivity.

Figure 65a–d shows the merging angle for the merging events that occurred in OL tests 60, 100, and 250 (no merging events were registered for OL-300). Merging angles were normalized to vary between 0 and 90° between the fractures. Angles in the range from 0 to 45° are called 'low angle,' while angles larger than 45° are referred to as 'high angle.' Merging angles are especially significant when there is an observable fracture path deflection in at least one of the fractures that merges, because it implies the stress field has exerted some influence on the deflection. Deflection is significant only in OL-100 (Fig. 65b), where fractures follow more curved trajectories. Both OL-60 (Fig. 65a) and OL-250 (Fig. 65c) have shorter fractures that are mostly straight, and there are no merging events in OL-300 that can make this variable relevant in that case.

Figure 7 shows sample gas production curves for OL tests. Here again we found a clustering effect on the curve slopes into low (OL-60 and OL-100) and high (OL-250 and OL-300) Bloom number. While the final produced gas volume totals about 40 cm^3 for all tests, the production rate is greater for the low Bloom number group. As observed in Fig. 3b, the bottle that holds the gelatin used to measure gas production is not subject to the same stress field as that inside the Hele-Shaw cell. Therefore, the gas production curves indicate that
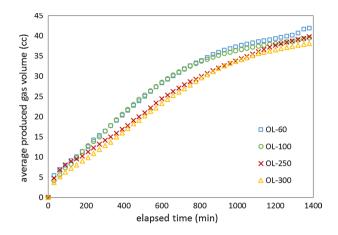
Fig. 7 Measured gas production for ordinary light (OL) tests

Table 2 Results summary for ordinary light tests

Property	Bloom number			
	60 (OL-60)	100 (OL-100)	250 (OL-250)	300 (OL-300)
Nucleation events	930	32	173	9
Distance nucleation to center (cm)	7	15	20	8
Fracture cumulative length (cm)	920	150	375	17
Average fracture length (cm)	0.99	4.68	2.16	1.88
Fracture density (#fractures/cm^2)	2.3	0.071	0.4	0.022
Max. fracture velocity (cm/s)	1×10^{-6}	5×10^{-6}	5×10^{-7}	8×10^{-7}
Max. average pressure (Pa)	2378.4	1127.5	4993.67	14,254.67
Length distribution skew	left	even	left	left
Coalescence angle distribution	even	high	high	N/A
Total gas production (cm^3)	42	38	30	35
Merging to nucleation ratio	0.54	0.81	0.45	N/A

all gelatins hold the potential to produce about the same amount of gas, but the array of the gelatin matrix matters to the point of inducing significant variability in the results.

Table 2 summarizes the average values of measured and calculated parameters for OL tests including nucleation events, fracture cumulative length, average distance of fracture nucleation site to center, fracture density, maximum fracture velocity and average pressure, gas production, and merging to nucleation ratio. The variables per se do not show a discernible trend. Thus they need to be explained within the context of the synergy of transport mechanisms previously discussed. Maximum average pressure, calculated using Eq. (3), shows an increasing trend with Bloom number, with the exception of Bloom 100 gelatin. In that case, maximum average pressure shows a decrease. This is due in part to the longer fractures developed in this sample. As the average fracture length values in Table 2 show, Bloom 100 gelatin has the largest number of all, more than twice the second largest value (Bloom 250). As Eq. (3) teaches, fracture propagation pressure is inversely proportional to fracture length. Thus, a very large cumulative fracture length overcame other

factors, such as gelatin fracture toughness, to ultimately decrease the maximum average pressure from what the trend would have predicted.

5.3.5 Polarized Light (PL) Tests

The stress field on the source rock matrix depends strongly on geomechanical factors such as Young's modulus and Poisson's ratio, and the analog material is no different. Fracture network development also has a corresponding effect on the stress field. The next steps involve studying the response of the fracture network to varying gelatin Young's modulus, as well as using photoelasticity principles that use gelatin birefringence to image the dynamics of the stress field and fracture propagation. The experimental observations described so far need to be complemented with the study of the transient stress field of the tests.

Photoelasticity tests were carried out as an exploratory step to help understand what to expect of the technique when applied to the experimental setup, as described in Fig. 3. To achieve this, the setup was fitted with polarizer filters at 90 degrees rotation difference between the light source and the Hele-Shaw cell, and on the camera lens. RGB images were acquired under the same parameters as the optical light experiments, but a smaller area was selected for imaging, in order to improve image resolution. Thus, final resolution achieved for all experiments oscillates between 0.26 and 0.30 mm/px. In order to improve visualization of the light intensity captured by each image, the original RGB format was converted to grayscale and a color map applied.
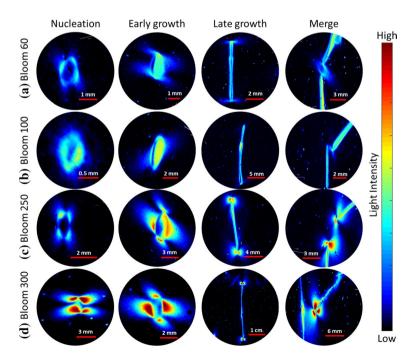

Fig. 8 Light intensity maps for selected areas from representative experimental birefringence images (polarized light tests)

Figure 8 shows grayscale light intensity maps for selected representative areas after processing during several stages of the fracture propagation test: nucleation, early growth, late growth and coalescence, for each gelatin strength tested. In Fig. 8, greater light intensity areas are on the red end of the colormap spectrum, while low light intensity or unfractured areas are darker. The image sequence shows that significant changes in light intensity occur as the test progresses. Here again, a clustering of results is observed in terms of low (60–100) and high (250–300) Bloom number. Low Bloom number gelatins (Fig. 8a, b) tend to exhibit smaller stress value ranges than their high Bloom number counterparts (Fig. 8c, d). At nucleation time, there is stress (proxied by light intensity) all around the nucleation site, and in the early stages of growth, the stress continues longitudinally and at the tip of the fractures. For small Bloom samples, stress seems to have a stronger presence on only one side of the fracture axis, while larger Bloom samples show stress development on both sides of the fracture. At late growth stages, stress locates mostly at the tip of the fractures, virtually disappearing from the fracture length. During fracture merging, a concentration of stress (via an increase in light intensity) is observed. Overall, it is observed that light intensity increases in magnitude with Bloom number in all the fracture propagation stages illustrated.

In order to estimate stress magnitude from photoelasticity images, fringe order must be determined from the original RGB format following the same procedure as for the fringe-stress factor calibration tests. RGB colors observed around the fractures were correlated to those tabulated in the referenced color sequence-fringe order table, and fringe orders were estimated for each sampled fracture. Using Eq. (33) and the f_σ values shown in Table 1, the experimental difference of principal stresses for each gelatin was estimated from a sample fracture and are plotted in Fig. 9.

6 Numerical Compared to Experimental Results

The sum of the results observed in Figs. 6, 7, and 8 indicate that the gas flow mechanisms that govern the fracture nucleation and propagation have a strong dependence on gelatin strength (proxy by Bloom number) and lead to distinct outcomes. Because all other factors
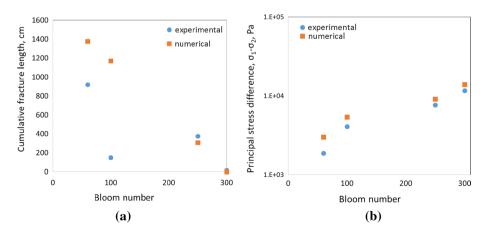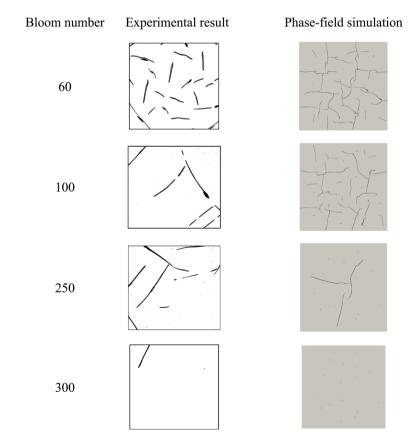

(a) **(b)**

Fig. 9 Comparison of experimental and numerical results: **a** cumulative fracture length and **b** principal stress difference. Note good agreement of principal stress differences

being equal, gelatin strength is a strong indicator of its predominant rheological behavior (viscoelastic spectrum), results seem to suggest that the gas flow mechanism that dominates the fracturing process is a function of gelatin rheology, in particular, its Young's modulus and diffusion coefficient. Additionally, the gelatin matrix stress field behaves dynamically with the fracture network development and interactively determines the final array of fractures that result in each test. Therefore, gas flow mechanism selectivity is also dependent on the transient behavior of the stress field, and the description below needs to be coupled with a stress field component. It is proposed that the most relevant gas transport mechanisms involved in this process are diffusion and deformation, and they are dominant at different degrees for each of our sample tests. It is also proposed that these mechanisms are subject to be inhibited at variable degrees by the gelatin fracture toughness K_c, which is in turn a function of its Young's modulus, as expressed by Eq. (3).

Figure 9 shows comparative plots of (a) cumulative fracture length and (b) estimated principal stress difference values calculated for numerical and experimental methods. Figure 10 shows numerical and experimental fracture network comparative results for gelatins of Bloom 60 to 300 on a 3 cm by 3 cm sub-domain. Comparing experimental and numerical results as presented in Figs. 9 and 10, a reasonable agreement is observed. Principal

Fig. 10 Experimental results compared to numerical results for evolved fracture network on gelatin in a 3 by 3 cm domain. Bloom number in the left column, experimental result in the center column after image analysis and binarization to identify fractures, and the simulated result in the right column
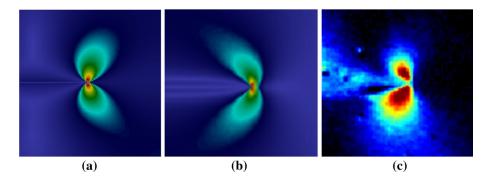
stress differences show acceptable agreement between experiments and numerical model results. In the numerical simulation, fracture networks seem to show coarser differentiation among Bloom numbers, with results tending to cluster into 'low' (60–100 Bloom) and 'high' (250–300 Bloom). This indicates that the general linear trend of the fracture network correlated with gelatin strength is being correctly captured by the numerical model. Some of the non-monotonic trend of the fracture density with Bloom number, Fig. 9a, was not captured, probably because the mechanical and flow parameters used in the numerical model are first-order linearized approximations of material behavior. The non-monotonic trend requires much more detailed material tests that are currently beyond our scope.

Figure 11 shows a qualitative comparison of (a) numerically generated stress fields for type I opening mode, (b) simulation using the experimental parameters, and (c) a representative example of stress-induced, experimentally acquired light intensity map similar to those shown in Fig. 8. Importantly, Fig. 11c displays the typical response found in early or late stages of fracture growth (depending on gelatin strength) within our image data set.

The orientation of model stress distribution and experimental photoelastic imaging (Fig. 11b, c) differ from that of classical model I fracture stress distribution as shown in Fig. 11a. Most literature refers to mode I as the default opening mode, but in the case where external force is applied to the crack inner boundary instead of a far-field force, the resulting stress distribution is significantly different. Importantly, notice the agreement between Fig. 11b and c, where the stress lobes and stress-induced fringes, respectively, incline toward the central portion of the fracture as compared to those shown in Fig. 11a, for type I mode, that incline toward the fracture tip.

Figure 12 shows additional numerical model results that are useful for comparison to experiments, specifically Fig. 8. Figure 12 shows the relative stress field at Bloom numbers of 60 and 100. Red is large stress and blue is low stress. As the Bloom number increases in Figs. 8 and 12, the stress concentration increases indicating consistency among the numerical and experimental results. Note that the Bloom 100 results in Fig. 12 show significant stress concentration at nucleation, early time, and late time stages as compared to Bloom 60. The merge events in Fig. 12 likewise show significant realism with stress concentration immediately before fractures join.

(a)	**(b)**	**(c)**

Fig. 11 Stress distribution at crack tip for **a** type I opening mode, **b** numerical model, and **c** stress-induced light intensity map for photoelastic experiments. Note the difference in the stress distribution when force is applied on the crack inner boundary in (**b**) and (**c**)
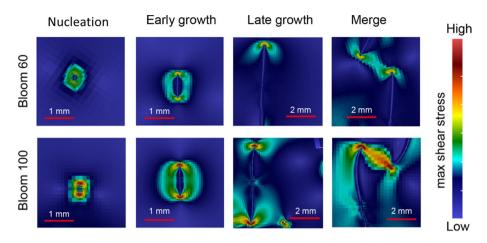
Fig. 12 Numerical results: Stress distribution at various stages during the fracture generation process

7 Future Work

The stress field on the source rock matrix depends strongly on geomechanical factors such as Young's modulus and Poisson's ratio. The analog material mimics these dependencies. Fracture network development also has a corresponding effect on the stress field. The results presented agree on this point. Further benchmarking of the numerical model and definition of the mechanisms that control fracture network development shall be conducted. We plan to refine further the numerical model implementation to be scalable to a large computation domain and extend the approach to 3D. This requires a faster linear solver and preconditioner for the iterative solver. We also want to incorporate the mechanism of interaction and merging with natural fractures. For fluid simulation, current Lagrange polynomial interpolation does not preserve fluid mass at the element level. Therefore, we plan to use the discontinuous Galerkin method to model multiphase flow to have better stability behavior for the transport problem. An unresolved experimental issue is extension of the gelatin verification data set to 3D because such experiments are difficult to visualize in real time.

8 Conclusions

Experimental and simulated stress fields reveal that fractures resulting from internal gas generation are similar to, but not identically, type I opening mode. The normal force applied on the fracture surface due to internal gas generation caused the stress concentration to distribute differently from classical type I. Importantly, the simulated and experimental fracture networks agree qualitatively and we have found that aspect ratio of the stress contour serves as a good indicator for the tendency of fracture propagation.

The numerical model proposed has shown that the phase-field fracture propagation approach has the capability to validate numerically the hypothesis derived from experimental observations that internal gas generation may generate fracture networks. Numerical benchmark tests were conducted to validate model accuracy. Along with birefringence

results, we demonstrated that fracture propagation in maturing gelatin analogs indeed results from internal pressure buildup. The agreement of the detailed fracture merging behavior showed the validity of the variational fracture criterion. Finally, we simulated the fracture network with random initial defects. The resulting fracture pattern indicated that the optimal fracture spacing and the number of drainage pathways are a strong function of the material elasticity parameter.

Using an experimental analog material as a proxy for source rock maturation allows for the sample to be imaged optically at time and length scales X-rays cannot achieve. Gelatin rheological behavior includes a brittle-elastic spectrum that approximates that of the brittle-elastic deformation of source rock. By observing the crack formation and propagation of the gelatin medium with internal gas generation provided by yeast fermentation, we characterize the experimental fracture network development and extract metrics that are translated into a corresponding numerical model. Image analysis of the series of repeatable laboratory-scale experiments revealed trends in fracture network development and characteristic parameters. The gelatin matrix stress field was inferred to exert strong influence on these observed results: nucleation sites, fracture orientation, fracture connection angles, and merging to nucleation ratios. The stress field is in turn dependent on the matrix rheological properties that for gelatin lay within a viscous-elastic spectrum that establishes the balance between gas transport mechanisms such as diffusion and deformation. The observed fracture network behavior was consistent with fracture mechanics predictions.

The mechanical properties of the gelatin vary with Bloom number that is a proxy for their Young's modulus. Based on the response obtained in the Hele-Shaw experiments, small Bloom numbers have a significant viscous response while greater Bloom numbers tend to display elastic behavior. Correlations were found between gelatin Bloom number (i.e., Young's modulus) and measured and calculated parameters such as fracture length, fracture velocity, angle of merging, fracture connectivity, and so on. Mechanisms include gas diffusion through the gelatin matrix and gas pressure-induced fracturing of the gelatin matrix. The predominance of one or the other mechanism varies nonlinearly with Bloom number.

Photoelasticty techniques and gelatin birefringence allowed for visualization of stress-induced light intensity variations around individual cracks and over whole fracture networks. At nucleation time, large stress areas were observed at the 'corners' around the nucleation site. As the fracture grows, high-stress zones were observed at the growing fracture tip(s) and across the fracture's length. After a particular fracture length, large stress zones are observed only at the fracture growing tip(s). Additional large stress is observed at the site and time of fracture merging. Stress magnitude increased with gelatin strength.

References

Allix, P., Burnham, A., Fowler, T., Herron, M., Kleinberg, R., Symington, B.: Coaxing oil from shale. Oilfield Rev. **22**(4), 4–15 (2011)

Ambrosio, L., Tortorelli, V.M.: Approximation of functional depending on jumps by elliptic functional via t-convergence. Commun. Pure Appl. Math. **43**(8), 999–1036 (1990)

American Association of Petroleum Geologists (AAPG). Kerogen; AAPG: Tulsa, OK, March 3, 2016. http://wiki.aapg.org/Kerogen

Amor, H., Marigo, J.J., Maurini, C.: Regularized formulation of the variational brittle fracture with unilateral contact: numerical experiments. J. Mech. Phys. Solids **57**(8), 1209–1229 (2009)

Anderson, E.R.: Propagation and Interaction of Pressurized Cracks in Photoelastic Gelatin. MS Thesis, Stanford University, Stanford, CA (1978)

Arvanitoyannis, I., Psomidau, E., Nakayama, A., Aiba, S., Yamamoto, N.: Edible films made from gelatin, soluble starch, and polyols, Part 3. Food Chem. **60**(4), 593–604 (1997)

Baek, T.H., Kim, M.S., Hong, D.P.: Fringe analysis for photoelasticity using image processing techniques. Int. J. Softw. Eng. Appl. **8**(4), 91–102 (2014). https://doi.org/10.14257/ijseia.2014.8.4.11

Bangerth, W., Hartmann, R., Kanschat, G.: A general-purpose object-oriented finite element library. ACM Trans. Math. Softw. **33**(4), 24 (2007)

Brace, W., Walsh, J., Frangos, W.: Permeability of granite under high pressure. J. Geophys. Res. **73**(6), 2225–2236 (1968)

Berg, R.R., Gangi, A.F.: Primary migration by oil-generation microfracturing in low-permeability source rocks: application to the Austin Chalk, Texas. AAPG Bull. **83**, 727–756 (1999)

Bloom, O.T.: U.S. Patent No. 1,540,979. Washington, DC: US Patent and Trademark Office (1925)

Bochev, P.B., Dohrmann, C.R., Gunzburger, M.D.: Stabilization of low-order mixed finite elements for the Stokes equations. SIAM J. Numer. Anal. **44**(1), 82–101 (2006)

Borja, R.I.: Plasticity: Modeling & Computation. Springer (2013)

Bostrom, N., Leu, G., Pomerantz, D., Machlus, M., Herron, M., Kleinberg, R.: Realistic oil shale pyrolysis programs: kinetics and quantitative analysis. Oil Shale Symposium (2009)

Bourdin, B., Francfort, G.A., Marigo, J.J.: Numerical experiments in revisited brittle fracture. J. Mech. Phys. Solids **48**(4), 797–826 (2000)

Bourdin, B., Francfort, G.A., Marigo, J.J.: The variational approach to fracture. J. Elast. **91**(1), 5–148 (2008)

Bourdin, B., Chukwudozie, C.P., Yoshioka, K.: A variational approach to the numerical simulation of hydraulic fracturing. In: SPE Annual Technical Conference and Exhibition. Society of Petroleum Engineers (2012)

Burnham, A.K., Singleton, M.F.: High pressure pyrolysis of green river oil shale. In: Geochemistry and Chemistry of Oil Shales, ACS Symposium Series 230. American Chemical Society (1983)

Burnham, A.K.: Chemistry and kinetics of oil shale retorting, in oil shale: a solution to the liquid fuel dilemma. In: ACS Symposium Series 1032, American Chemical Society (2010)

Capuano, R.M.: Evidence of fluid flow in microcracks in geopressured shales. AAPG Bull. **77**, 1303–1314 (1993)

Charmette, C., Sanchez, J., Gramain, Ph, Rudatsikira, A.: Gas transport properties of poly(ethylene oxide-co-epichlorohydrin) membranes. J. Membr. Sci. **230**, 161–169 (2004). https://doi.org/10.1016/j.memsci.2003.10.043

Chen, Z., Bunger, A.P., Zhang, X., Jeffrey, R.G.: Cohesive zone finite element-based modelling of hydraulic fractures. Acta Mech. Solida Sin. **22**(5), 443–452 (2009)

Chukwudozie, C., Bourdin, B., Yoshioka, K.: A variational phase-field model for hydraulic fracturing in porous media. Comput. Methods Appl. Mech. Eng. **347**, 957–982 (2019)

Dally, J., Riley, W.: Experimental Stress Analysis, 3rd edn. McGraw-Hill, New York (1991)

Di Giuseppe, E., Funiciello, F., Corbi, F., Ranalli, G., Mojoli, G.: Gelatins as rock analogs: a systematic study of their rheological and physical properties. Tectonophysics **473**(3–4), 391–403 (2009)

du Rouchet, J.: Stress fields, a key to oil migration. AAPG Bull. **65**, 445–459 (1981)

Erdogan, F., Sih, G.C.: On the crack extension in plates under plane loading and transverse shear. J. Basic Eng. **85**(4), 519–525 (1963)

Glatz, G., Castanier, L.M., Kovscek, A.R.: Visualization and quantification of thermally induced porosity alteration of immature source rock using X-ray computed tomography. Energy Fuels **30**(10), 8141–8149 (2016). https://doi.org/10.1021/acs.energyfuels.6b01430

Glatz, G., Lapene, A., Castanier, L.M., Kovscek, A.R.: An experimental platform for triaxial high-pressure/high-temperature testing of rocks using computed tomography. Rev. Sci. Instrum. **89**, 045101 (2018). https://doi.org/10.1063/1.5030204

Griffith, A.: The phenomena of rupture and flow in solids. Royal Society of London. Series A. **221**, 163–198 (1921)

Francfort, G.A., Marigo, J.J.: Revisiting brittle fracture as an energy minimization problem. J. Mech. Phys. Solids **46**(8), 1319–1342 (1998)

Heister, T., Wheeler, M.F., Wick, T.: A primal-dual active set method and predictor-corrector mesh adaptivity for computing fracture propagation using a phase-field approach. Comput. Methods Appl. Mech. Eng. **290**, 466–495 (2015)

Hintermüller, M., Ito, K., Kunisch, K.: The primal-dual active set strategy as a semismooth newton method. SIAM J. Optim. **13**(3), 865–888 (2002)

Hubbert, M.: Theory of scale models as applied to the study of geologic structures. Bull. Geol. Soc. Am. **48**(10), 1459–1517 (1937)

Irwin, G.: Fracture dynamics. Fracturing of Metals, 152 (1948)

Ji, S.H., Park, Y.J., Lee, K.K.: Influence of fracture connectivity and characterization level on the uncertainty of the equivalent permeability in statistically conceptualized fracture networks. Transp. Porous Media **87**(2), 385–395 (2011)

Jiang, J., Yang, J.: Coupled fluid flow and geomechanics modeling of stress-sensitive production behavior in fractured shale gas reservoirs. Int. J. Rock Mech. Min. Sci. **101**, 1–12 (2018)

Ju, Y., Zheng, Z., Xie, H., Wang, L., He, K.: Experimental visualization methods for three-dimensional stress fields of porous solids. Exp Tech. **41**, 331–344 (2017)

Kavanagh, J.L., Menand, T., Sparks, R.S.J.: An experimental investigation of sill formation and propagation in layered elastic media. Earth Planet. Sci. Lett. **245**, 799–813 (2006)

Kavanagh, J.L., Menand, T., Daniels, K.A.: Gelatine as a crustal analogue: determining elastic properties for modelling magmatic intrusions. Tectonophysics **582**, 101–111 (2013)

Kavanagh, J.L., Boutelier, D., Cruden, A.R.: The mechanics of sill inception, propagation and growth: experimental evidence for rapid reduction in magmatic overpressure. Earth Planet. Sci. Lett. **421**, 117–128 (2015)

Kobchenko, M., Hafver, A., Jettestuen, E., Renard, F., Galland, O., Jamtveit, B., Meakin, P., Dysthe, D.K.: Drainage fracture networks in elastic solids with internal fluid generation. Europhys. Lett. **102**, 66002 (2013)

Kobchenko, M., Hafver, A., Jettestuen, E., Renard, F., Galland, O., Jamtveit, B., Meakin, P., Dysthe, D.K.: Evolution of a fracture network in an elastic medium with internal fluid generation and expulsion. Phys. Rev. E **90**(052801), 1–9 (2014)

Lash, G.G., Engelder, T.: An analysis of horizontal microcracking during catagenesis: example from Catskill delta complex. AAPG Bulletin **89**, 1433–1449 (2005)

Le-Doan, T.-V., Bostrom, N.W., Burnham, A.K., Kleinberg, R.L., Pomerantz, A.E., Allix, P.: Experimental study of green river oil shale pyrolisis. SPE paper 168715 presented at the Unconventional Resources Technology Conference (URTeC) held in Denver, CO. Aug. 12-14 (2013)

Lee, S., Mikelic, A., Wheeler, M.F., Wick, T.: Phase-field modeling of proppant-filled fractures in a poroelastic medium. Comput. Methods Appl. Mech. Eng. **312**, 509–541 (2016)

Lee, S., Mikelic, A., Wheeler, M.F., Wick, T.: Phase-field modeling of two phase fluid filled fractures in a poroelastic medium. Multisc. Model. Simul. **16**(4), 1542–1580 (2018)

Li, F.: Study of Stress Measurement Using Polariscope. PhD Thesis, Georgia Institute of Technology, Atlanta, GA (2010)

Mauthe, S., Miehe, C.: Hydraulic fracture in poro-hydro-elastic media. Mech. Res. Commun. **80**, 69–83 (2017)

Márquez, X.M., Mountjoy, E.W.: Microcracks due to overpressures caused by thermal cracking in well-sealed Upper Devonian reservoirs, deep Alberta basin. AAPG Bull. **80**, 570–588 (1996)

McCarthy, K., Rojas, K., Niemann, M., Palmowski, D., Peters, K., Stankiewicz, A.: Basic petroleum geochemistry for source rock evaluation. Oilfield Rev. **23**, 2 (2011)

Miehe, C., Welschinger, F., Hofacker, M.: Thermodynamically consistent phase-field models of fracture: variational principles and multi-field fe implementations. Int. J. Numer. Methods Eng. **83**(10), 1273–1311 (2010a)

Miehe, C., Hofacker, M., Welschinger, F.: A phase-field model for rate independent crack propagation: robust algorithmic implementation based on operator splits. Comput. Methods Appl. Mech. Eng. **199**(45), 2765–2778 (2010b)

Mohammadnejad, T., Andrade, J.E.: Numerical modeling of hydraulic fracture propagation, closure and reopening using xfem with application to in situ stress estimation. Int. J. Numer. Anal. Methods Geomech. **40**(15), 2033–2060 (2016)

Özkaya, I.: A simple analysis of oil-induced fracturing in sedimentary rocks. Mar. Pet. Geol. **5**, 293–297 (1988)

Phillips, J.W.: Experimental Stress Analysis. Ch. 6. http://www.ifsc.usp.br/~lavfis/images/BDApostilas/ApEfFotoelastico/photoelasticity.pdf. Accessed 4 Dec 2017 (2008)

Ramesh, K.: Digital Photoelasticity. Advanced Techniques and Applications. Springer Berlin Heidelberg, Berlin (2000)

Ross-Murphy, S.: Structure and rheology of gelatin gels: recent progress. Polymer **33**(12), 2622–2627 (1992)

Sigma-Aldrich. Gelatin Product Information Sheet, CAS RN 9000-70-8. https://www.sigmaaldrich.com/content/dam/sigma-aldrich/docs/Sigma/Product_Information_Sheet/2/g9382pis.pdf. Accessed 21 Feb 2018

Takada, A.: Experimental study of propagation of liquid-filled crack in gelatin: shape and velocity in hydrostatic stress condition. J. Geophys. Res. **95**(B6), 8471–8481 (1990)

Takada, A.: Accumulation of magma in space and time by crack interaction. In: Ryan, M.P. (ed.) Magmatic Systems, pp. 241–257. Academic Press, San Diego (1994)

Talukdar, S., Gallango, O., Vallejos, C., Ruggiero, A.: Observations on the primary migration of oil in the La Luna source rocks of the Maracaibo Basin, Venezuela. Oil Gas Sci. Technol. Rev. IFP. **43**(3), 357–370 (1988)

Tanné, E., Li, T., Bourdin, B., Marigo, J.J., Maurini, C.: Crack nucleation in variational phase-field models of brittle fracture. J. Mech. Phys. Solids **110**, 80–99 (2018)

ten Grotenhuis, S.M., Piazolo, S., Pakula, T., Passchier, C., Bons, P.D.: Are polymers suitable rock analogs? Tectonophysics **350**, 35–47 (2002)

Timoshenko, S., Goodier, J.: Theory of Elasticity. McGraw-Hill Higher Education, New York (1970)

van Otterloo, J., Cruden, A.R.: Rheology of pig skin gelatine: defining the elastic domain and its thermal and mechanical properties for geological analogue. Tectonophysics **683**, 86–97 (2016)

Vishay Precision Group. Introduction to Analysis by the PhotoStress Method. Tech Note TN-702-2 (2011)

Watanabe, T., Masuyama, T., Nagaoka, K., Tahara, T.: Analog experiments on magma-filled cracks: competition between external stresses and internal pressure. Earth Planets Space **54**, 1247–1261 (2002)

White, J.A., Borja, R.I.: Stabilized low-order finite elements for coupled solid deformation/fluid-diffusion and their application to fault zone transients. Comput. Methods Appl. Mech. Eng. **197**(49–50), 4353–4366 (2008)

White, J.A., Castelletto, N., Tchelepi, H.A.: Block-partitioned solvers for coupled poromechanics: a unified framework. Comput. Methods Appl. Mech. Eng. **303**, 55–74 (2016)

Wu, Y.S., Ye, M., Sudicky, E.A.: Fracture-flow-enhanced matrix diffusion in solute transport through fractured porous media. Transp. Porous Media **81**(1), 21 (2010)

Affiliations

B. Vega[1] · **J. Yang**[1] · **H. Tchelepi**[1] · **A. R. Kovscek**[1]

1   Energy Resources Engineering, Stanford University, Stanford, CA, USA